

# Quantum capacitance, and its screening, in an electrostatically floating Andreev bound state

Filip K. Malinowski,<sup>1,\*</sup> Damaz de Jong,<sup>1</sup> Lin Han,<sup>1</sup> Christian G. Prosko,<sup>1</sup>  
Michael Chan,<sup>1</sup> Luka Pavešič,<sup>2</sup> Rok Žitko,<sup>2</sup> Zoltán Guba,<sup>3</sup> R. K. Rupesh,<sup>4</sup> Yu Liu,<sup>5</sup>  
Peter Krogstrup,<sup>5</sup> Leo P. Kouwenhoven,<sup>1,6</sup> Andras Pályi,<sup>3</sup> and Jonne V. Koski<sup>6</sup>  
<sup>1</sup>*QuTech and Kavli Institute of Nanoscience, Delft University of Technology, 2600 GA Delft, The Netherlands*  
<sup>2</sup>*Jožef Stefan Institute & Faculty of Mathematics and Physics, University of Ljubljana, Ljubljana, Slovenia*  
<sup>3</sup>*Department of Theoretical Physics & MTA-BME Exotic Quantum Phases Research Group, Budapest University of Technology and Economics, H-1111 Budapest, Hungary*  
<sup>4</sup>*School of Physics, University of Hyderabad, Telangana 500046, India*  
<sup>5</sup>*Center for Quantum Devices, Niels Bohr Institute, University of Copenhagen & Microsoft Quantum Materials Lab Copenhagen, Lyngby, Denmark*  
<sup>6</sup>*Microsoft Quantum Lab Delft, Delft University of Technology, 2600 GA Delft, The Netherlands*  
(Dated: March 7, 2022)

We study the response of a resonator attached to a gate of a floating quantum dot coupled to a superconducting island, defined in an InAs nanowire with an epitaxial Al shell. Thanks to fixing the total charge we prevent the system from undergoing a singlet-doublet transition and explore regime not accessible in conventional transport measurements. We find that radio-frequency reflectometry signal distinguishes between the superconducting island hosting no subgap states and discrete subgap states. In the case of the superconducting island hosting no subgap states we vary the tunnel coupling. For small tunnel coupling, when the gap to the quasi-continuum of the excited states is small, the thermal excitations suppress the quantum capacitance. The resonance frequency shift and changes in the quality factor at the charge transitions are simulated using a projected numerical renormalization group method, and show good quantitative agreement with the experiment. The established measurement method, as well as the analysis and simulation framework, are suitable for the study of devices consisting of multiple superconducting islands and quantum dots, such as Andreev molecules or a Kitaev chain.

## INTRODUCTION

Andreev bound states (ABSs), and closely related Yu-Shiba-Rusinov states, are discrete fermionic states in a superconductor, with an energy lower than the superconducting gap [cn]. They can be localized in weak superconducting links[1], Josephson junctions[2][cn], at sites of impurities [cn] or in semiconducting quantum dots coupled to a superconductor[3, 4]. ABSs are similar to discrete electronic states in a quantum dot, in that they are well localized in space and, depending on occupancy, may have a spin which can be manipulated[5, 6]. But they also differ, in that the superconducting interaction couples states with a charge differing by  $2e$ [cn]. Consequently, rather than referring to the absolute occupancy of the bound states, it only is only meaningful to refer to the parity of the ABS, whether it is even- or odd-occupied. Which of these is the true ground state depends on the microscopic details of the system. In case of the ABS formed in a quantum dot coupled to a superconducting lead, the ground state parity changes depending on the dot-superconductor coupling, charging energy, energy of the dot orbitals etc.[3, 4]

When the superconducting lead is substituted by a small superconducting island (with a charging en-

ergy larger than the temperature,  $E_C \gg kT$ ) the picture changes subtly[7], especially if the total number of charges is fixed. Changing the ABS parity requires paying the additional energy of a superconducting gap  $\Delta$ , since the excess quasiparticle remains confined to the quasi-continuum of states in the superconducting island[8, 9]. Consequently the ABS parity in the ground state never changes – the system does not undergo singlet-doublet phase transition – enabling access to the regime inaccessible in a conventional transport measurement. Tuning the ABS parameters can now only affect the gap size between the discrete ground state, and the quasi-continuum of the excited states (Fig. 1(c)).

In this work we study an Andreev bound state formed in a gate-tunable quantum dot coupled to a superconducting island (Fig. 1(a,c,d)), in the electrostatically floating configuration, i.e. with the total fixed charge of the coupled dot-island system. By definition, such a configuration does not allow to perform transport measurements. Instead, our approach is to couple the quantum dot capacitatively to the superconducting resonator (Fig. 1(a,b)), and study the resonator frequency shift and quality factor as a function of different gate voltages and the external magnetic field.

First, we show a qualitative difference in the resonator response between the cases of the dot coupled to the superconducting island within which there exists or does not exist a discrete subgap state. Having ensured there is no subgap states in the island, we study the effective

---

\* f.k.malinowski@tudelft.nl

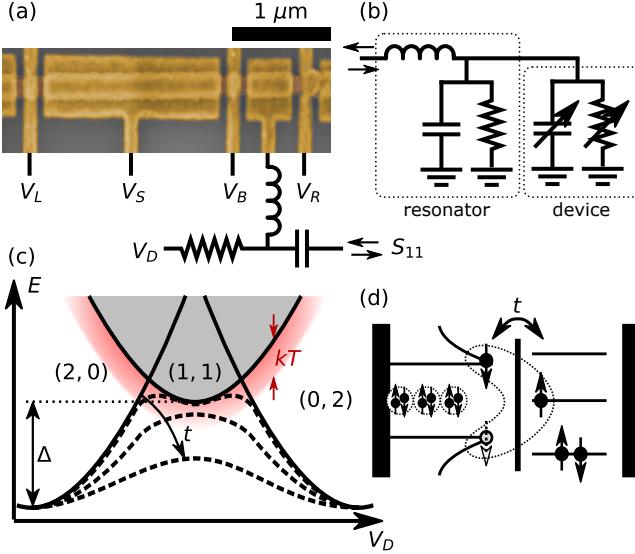


FIG. 1. (a) False-colored SEM of the device nominally identical to the one measured, schematically illustrating the resonator circuit with a bias-tee. (b) An equivalent resonator circuit. Fixed inductance, capacitance and inductance represent the spiral inductor resonator, while the variable capacitance and resistance represent the loading of the resonator due to quantum capacitance and losses in the coupled dot-island system. (c) Schematic energy diagram illustrating the evolution of the discrete ground state with increasing tunnel coupling. The shaded area represents a quasi-continuum of states, with an unpaired quasiparticle on the superconducting island. (d) Cartoon illustrating the density of states in a superconducting island, and their coupling to the quantum dot. The combination of the tunnel coupling and superconductivity leads to a formation of the well defined, discrete ground state.

capacitance of the ABS formed in the quantum dot, and show that the shape of the dot-island charge transition witnesses the magnitude of the tunnel coupling, and the size of the gap to the quasi-continuum. Using the using projected numerical renormalization group method we model the energy diagram of the lowest-lying eigenstates, and show that the capacitive response of the dot-island predominantly originates from the charge dispersion of the ABS, while the added dissipation is due to Sisiphus resistance. Next, we investigate the resonator response to reduction of the superconducting gap  $\Delta$  in the superconducting island, which we achieve by applying the external magnetic field. Finally, we show the dramatic change in the resonator response once the superconducting gap closes, and the island becomes normal.

## DEVICE

The device under study consists of the InAs nanowire with 2-facet Al epitaxial shell [10] partially etched away (Fig. 1(a)). The wrapped Ti/Au gates are used to elec-

trostatically define two quantum dots. The left dot,  $1.8 \mu\text{m}$  long, with Al not etched away, is operated as a superconducting island (unless mentioned otherwise), and tuned by a gate voltage  $V_S$ . The right dot,  $500 \text{ nm}$  long, is not covered by aluminum, and is tuned by the gate voltage  $V_D$ . The middle barrier gate voltage  $V_B$  controls tunnel coupling between the dots. The side barrier gate voltages  $V_{L/R}$  are set to large negative values which fixes a total charge on the double dot, on a timescale of several seconds to hours.

The dot plunger gate is attached to the off-chip spiral inductor resonator [11] ( $L = 570 \text{ nH}$ ,  $f_0 \approx 368 \text{ MHz}$ ,  $Q_{int} \approx 4000$ ,  $Q_{ext} \approx 285$ ). Near the interdot charge transition the movement of charges between quantum dots is enabled, loading the resonator with an additional capacitance  $C$  and effective conductance  $G$  (Fig. 1(b)). The resonator loading is reflected as a shift of the resonant frequency  $f_0$  and reduction of the internal quality factor  $Q_{int}$  (Appendix A).

## SUBGAP VS NO SUBGAP

In order to study of the ABS formation in the quantum dot we need to first ensure that there are no additional subgap states formed in the superconducting island itself. For that purpose we compare resonator response for three different tunings of the device (Fig. 2).

First, the superconducting plunger gate is set to large negative value  $V_S \approx -2 \text{ V}$ , which should fully deplete the semiconductor wire under the aluminum shell, eliminating all undesired subgap states [cn]. Meanwhile, the barrier gate is set to moderately negative values, preventing strong hybridization between the superconducting island and the quantum dot. Fig. 2(a) presents charge stability diagram in such a tuning, revealing alternating narrow and wide charge stability regions. The interdot charge transitions are highly asymmetric, with sharp edge on the side of the narrower charge stability regions.

Second, we increase the barrier gate voltage  $V_B$ , while keeping  $V_S \approx -2 \text{ V}$ , to enhance the hybridization between the quantum dot and superconducting island. The resulting charge stability diagram (Fig. 2(b)) has the same periodicity as in the first case, but lacks an alternating pattern of charge stability regions. The number of interdot charge transitions is halved, the transitions are symmetric, and added capacitance at the charge transition is significantly increased.

Third, we set  $V_S \approx 0.25 \text{ V}$ , which should lead to partial accumulation of the carriers under the aluminum shell and formation of additional bound states in the superconducting island. The corresponding charge stability diagram (Fig. 2(c)) reveals alternating pattern of stability regions. While not perfectly symmetric, the charge transitions lack the extreme asymmetry of those in Fig. 2(a), and are characterized by much greater added capacitance.

We interpret that wider (narrower) stability regions in

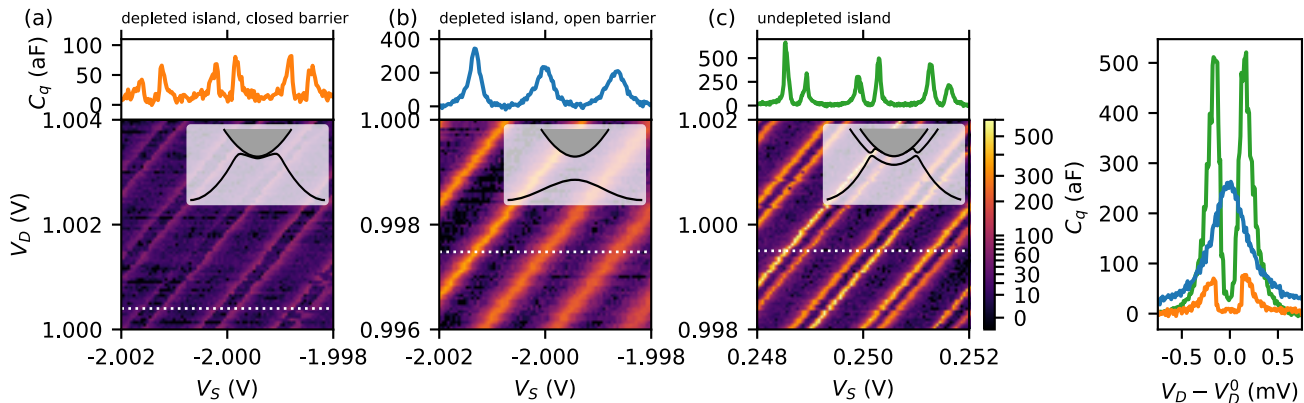


FIG. 2. Effective  $C$  a floating dot-island revealing the charge stability diagrams. Panels (a-c) represent three regimes: (a) depleted semiconductor under aluminum shell and small tunnel coupling; (b) depleted semiconductor and large tunnel coupling; (c) undepleted semiconductor under the aluminum shell. Shared power-law normalization of color maps was chosen to enable direct comparison of datasets. Top panels show the cut through the data, and insets illustrate schematically the energy diagram in each regime (cf. Fig. 1(c)). (d) Zoom in at an individual charge transition, or pair of charge transitions in the three regimes. The colors used for plotting the data correspond to the colors used in the top panels of (a-c).

Fig. 2(a,c) correspond to even-occupied (odd-occupied) superconducting island, with an individual electron is moved at the charge transitions. Meanwhile in (b) all stability regions correspond to even-occupied island, and electron pairs are exchanged at each charge transitions.

Insets in Fig. 2(a-c) present energy diagrams illustrating out interpretation of the data. In Fig. 2(c) the charge transitions result from tunneling of an individual electron between a quantum dot and a discrete subgap state on a superconducting island [12]. Since both involved state are well separated from the next excited states, the transition has virtually the same character as transition between two quantum dots. On the contrary, in Fig. 2(a), the quasi-continuum of excited states is within  $\sim kT$  of the ground state in the narrower charge stability regions. This enables thermal excitation of the quasiparticle from the discrete state to the continuum, which suppresses the quantum capacitance and leads to sharp edge of the charge transition. However, if the dot-island coupling is large enough, the bound state formed in the dot is always well separated from quasi-continuum (Fig. 1(c)). The result is the absence of the narrower stability regions in Fig. 2(b). Next, we study in detail the transition regime between weak and strong coupling of the quantum dot and superconducting island, including quantitative modeling of  $C_q$ .

### GRADUAL INCREASE OF THE TUNNEL COUPLING

To study vanishing of the narrower charge stability regions we fix the island gate voltage  $V_I = 2$  V, and measure charge stability diagram, with fixed probe frequency, with respect to dot and barrier gate voltages,  $V_D$  and  $V_B$  (Fig. 3). In particular, a range if  $V_B$  is chosen so that

resonance under the barrier gate allows to considerably tune the tunnel coupling, with only a small changes of  $V_B$ . We note that due to telegraph noise, presumably from a nearby two level system (TLS), the Fig. 3(b) is a composite of several repetitions of the measurement, all in identical range of voltages. Compositing procedure is described in Appendix XXX, and complementary analysis of the data for the other state of the TLS is presented in Appendix XXX.

Focusing on evolution of the individual charge transition (pair), we observe the shrinking and vanishing of the narrower charge stability region with increasing  $V_B$ , highlighted by taking a line cuts through the charge stability diagram (Fig. 3(b)). As the narrower charge stability region shrinks, the magnitude  $C$  at the charge transition increases, and is the highest as the pair of charge transitions merges.

The intuitive understanding of the narrower charge stability region can be provided by an analogy to the singlet-dublet quantum phase transition in case of the quantum dot coupled to the grounded superconductor [cn]. In that case the quantum dot charging energy  $U$  competes with the tunnel coupling  $\Gamma_S$  to the superconducting lead. As the chemical potential  $\varepsilon$  of the quantum dot is tuned, large charging energy favors increase of the dot one electron at the time, switching from the even-occupied singlet ground state, to odd-occupied dublet, and back to singlet. On the contrary – the large tunnel coupling favors addition of two electrons, by directly coupling singlet states, different by 2 electrons, via an Andreev reflection.

In case of the floating dot-island system, the true quantum phase transition of the ground state does not occur, as the total charge is fixed and the total parity – conserved. Nonetheless, the parity of the Andreev bound state formed in the dot may change, provided a sufficient

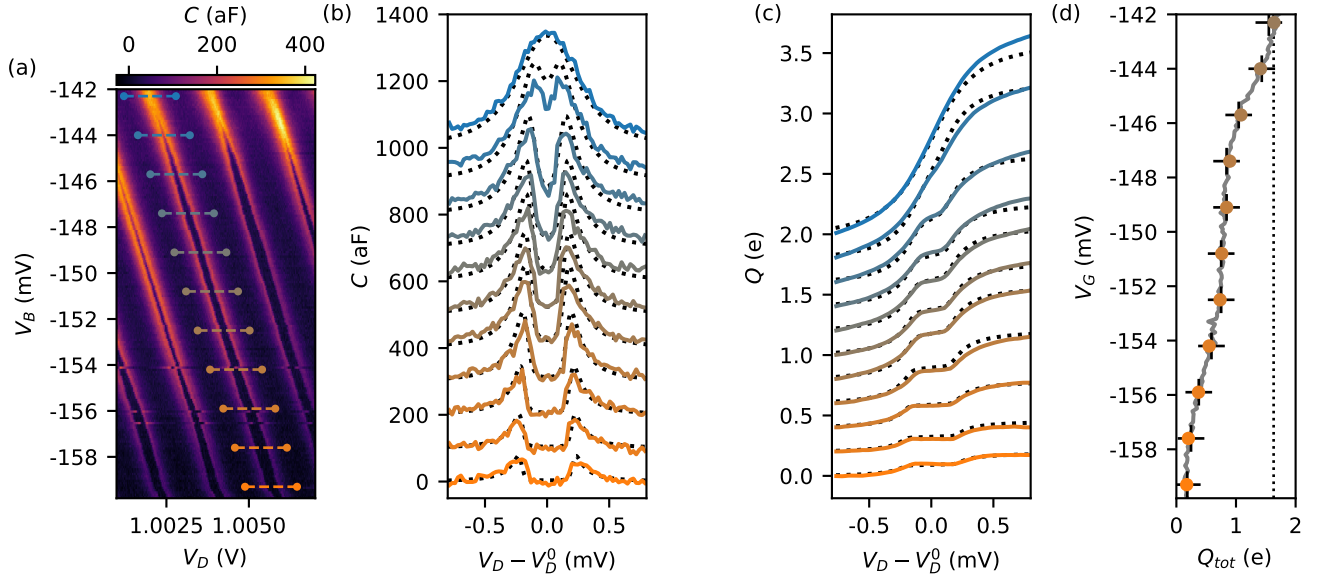


FIG. 3. (a) A charge stability diagram illustrating shrinking and vanishing of the charge stability regions with an odd-occupied island. The dashed line indicate the cuts through the data processed in panels (b-d). (b) Cuts through the data in (a). Solid, colored lines present the experimental data, and dotted black lines – the fit result. Curves are offset vertically for clarity. (c) The integral of the capacitance from  $V_D - V_D^0 = 0$  to a finite value. Solid, colored lines present the experimental data, and dotted black lines – the fit result. (d) Signature charge of the charge transition (pair) as a function of  $V_B$ . Colored points correspond to the line cuts and data in (a-c), and black crosses – the corresponding signature charge extracted from the model. Dotted line illustrates the value of  $2\alpha e$ , with the lever arm  $\alpha$  extracted from the measurement of the Coulomb diamonds.

amount of energy is provided for a single quasiparticle to occupy the quasicontinuum of the states above the superconducting gap. As illustrated in Fig. 1(c), for sufficiently small coupling the quasicontinuum can be separated from the discrete ground state by minigap  $\delta \leq k_B T$ . Whenever this condition is fulfilled, the system is excited to the quasicontinuum, which has high multiplicity and does not couple to the resonator. We interpret that the narrower stability regions, and their vanishing illustrated in Fig. 3(a,b), are due to such a thermal excitation, which we will refer to as a thermal suppression of the capacitance.

In the following, we proceed to model the capacitance and its suppression to support our interpretation.

### MODELING THE CAPACITANCE AND ITS THERMAL SUPPRESSION

For modeling of the signal we employ a single impurity Anderson model [cn]. After projection to fixed parity subspace (XXX how is charge fixed?), the Hamiltonian takes form

$$\begin{aligned} \hat{H} = & \varepsilon \hat{n} + U n_{\downarrow} n_{\uparrow} + \sum_k \varepsilon_k \\ & + \sum_k \left( \Delta c_{k\uparrow}^\dagger c_{k\uparrow}^\dagger + \text{H.c.} \right) \\ & + \sum_{k,\sigma} \left( V c_{k\sigma}^\dagger d_\sigma + \text{H.c.} \right), \end{aligned} \quad (1)$$

where  $d_\sigma$  and  $\hat{n}_{(\sigma)}$  are annihilation and electron number operators for the impurity, and spin  $\sigma$ .  $c_{k\uparrow}$  is the annihilation electron for the electron on the  $k$ -th island orbital, with energy  $\varepsilon_k$ .  $\varepsilon = \alpha V_D$  is the energy detuning of the impurity level;  $U$  – charging energy of the impurity, effectively equal to the sum of dot and island charging energies;  $\Delta$  – the BCS order parameter;  $V$  – impurity bath hopping. The model is solved using the Projected Numerical Renormalization Group (PNRG) [cn] to obtain the low-energy excitation spectra, expected value of charge for the lowest energy states, as well as static and dynamical charge susceptibility [cn].

Before attempting to match the simulations with the experimental results, we inspect the dynamical susceptibility in the model as a function of frequency [cn]. The simulations show the presence of a large gap in a dynamical susceptibility. Consequently, for used resonator frequency ( $f_0 \approx 368$  MHz) and device parameters, the static charge susceptibility is a suitable approximation, and we are indeed in a quantum-capacitance limit of circuit quantum electrodynamics. This approximation

holds for all our data, except near the gap closing in the magnetic field sweeps, which will be discussed later.

To model the quantum capacitance contribution we extract from the model we use the calculated ground state charge susceptibility  $\chi_g$ , and susceptibility of the lowest excited state in quasi-continuum  $\chi_e$ , separated by a quasi-gap  $\delta$ . For simplicity, instead of considering multiple states in quasi-continuum, we assume the multiplicity  $N$  of the lowest excited state, and we expect that  $N \lesssim 10^8$  (approximate number of Al atoms composing a superconducting shell). Quantum capacitance contribution to the signal is therefore given by

$$C_q = \chi_g P_g + (1 - P_g) \chi_e, \quad (2)$$

where  $P_g = (1 + N e^{-\delta/k_B T})^{-1}$  is the equilibrium occupancy of the ground state at temperature  $T$ . Since  $\chi_e$  is much smaller than  $\chi_g$ , this implies that for  $\delta \lesssim k_B T$  the quantum capacitance is suppressed.

To model the tunneling capacitance contribution we assume a zero-temperature relaxation rate  $\Gamma$ .  $\Gamma$  governs the redistribution of the occupancy between ground state and excited states over a period of a sinusoidal gate excitation (Appendix XXX). The resulting tunneling capacitance is given by

$$XXX. \quad (3)$$

We begin the comparison between the experiment and model by performing the fit to the cuts in Fig. 3(b), only taking into account the quantum capacitance contribution. In the simultaneous fit to all curves we use a fixed value of  $\Delta = 250 \mu\text{eV}$ , single value of  $U$ ,  $\alpha$  and  $T$ , and separate value of  $\Gamma_t$  for each cut. Due to computational complexity of PNRG calculations, the optimization is done on a discrete set of  $U$  and  $\Gamma_t$  values. The fit results are presented with black dashed lines in Fig. 3(b-d).

XXX

## I. CHARGE SIGNATURE OF THE TRANSITIONS

In Fig. 3(c) we integrate numerically the measured capacitance from the center of the charge transition (pair)  $V_D^0$  to  $V_D$

$$Q(V_D) = \int_{V_D^0}^{V_D} C(V'_D) dV'_D, \quad (4)$$

and in Fig. 3(d) we present the integral of capacitance across the full charge transition pair  $Q_{tot}$ . These two quantities will be used to quantify to what extent the system is trapped in a state that does not contribute to the measured capacitance.

XXX

In the effective capacitance picture,  $C$  consists of two contributions – so-called quantum and tunneling capacitance. [cn]

Quantum capacitance is the contribution that arises from the adiabatic response of the system to the oscillating AC voltage on the gate attached to the resonator. One can consider this contribution, by considering each eigenstate of the system, labeled by subscript  $i$ , with energy  $E_i(V_D)$ , to be occupied with certain probability  $p_i(V_D)$ . Collectively they contribute

$$C_q(V_D) = \sum i p_i \frac{d^2 E}{dV_D^2} = \sum i p_i \frac{dQ_i}{dV_D} = \alpha \sum i p_i(V_D) C_i. \quad (5)$$

Here,  $Q_i(V_D)$  represents the expected value of charge on a dot for  $i$ -th eigenstate,  $\alpha$  – a lever arm between the dot and the gate, and  $C_i$  – capacitance associated with each eigenstate. In particular, if ground state is occupied with probability  $p_0(V_D) = 1$  (at zero temperature), it immediately follows that

$$\int_{V_D^A}^{V_D^B} C_q(V'_D) dV'_D = \alpha (Q_0(V_D^B) - Q_0(V_D^A)). \quad (6)$$

In particular, integrating between the middle of the stability regions with charge different by  $2e$  should yield  $Q_{tot} = 2\alpha e$ .

On the other hand, the tunneling capacitance results from redistribution of  $p_i$  between the eigenstates over a single period of an AC excitation, and is affected by a rate at which the reaches the thermal equilibrium, relative to the drive frequency. In particular, in the limit of the equilibration rate being much greater than the drive frequency

$$C(V_D) = \alpha \frac{d\langle Q(V_D) \rangle}{dV_D}, \quad (7)$$

where  $\langle Q(V_D) \rangle$  represents the average dot charge in thermal equilibrium. Also in this case integrating between the middle of the stability regions with charge different by  $2e$  should yield  $Q_{tot} = 2\alpha e$ .

For our experiment, we conclude that the reduction of  $Q_{tot}$  below value of  $2\alpha e$  can be attributed to the system being trapped in an excited state, and unable to respond to the gate voltage changes at a timescale compared to the period of a drive frequency. Gradual increase of  $Q_{tot}$  from nearly 0 to  $Q_{tot} \approx 2\alpha e$  shows that the suppression of the signal by excitation of the system to quasi-continuum occurs to the lesser extent. As illustrated in Fig. 1(c)), this is due to the tunnel coupling increasing the energy gap between the discrete and the quasi-continuum, making the limit  $T \rightarrow 0$  increasingly adequate.

## OUTLOOK

To summarize, we establish a measurement method for studying an Andreev bound states in quantum dots that does not require transport through the device. In

quantum dots, such a capability enabled development of large dot arrays and multiqubit manipulation. We envision, that the dispersive sensing will enable tuning arrays and chains of ABSs, which so far were two- [13–17], or at most three-sites long [18]. A particularly appealing direction to pursue, using ABSs as building blocks, is a construction of the synthetic Kitaev chain [19–21], in which a topological superconductivity is predicted to emerge. In contrast to realizing topological superconductivity in nanowires or long Josephson junctions, Kitaev chain approach enables one to know tune the potential along the chain in a controllable manner. In a process of tuning such a long chain, the quantum capacitance measurements with a gate could be used to measure local compressibility, which can be used as a signature of whether the chemical potential of individual dots is tuned correctly [22].

## AUTHOR CONTRIBUTIONS

FKM performed the experiment and processed the experimental data. LP and RZ solved the Anderson impurity model. ZG, RKR and AP developed framework describing the thermal screening and dissipation, and performed the fits to the data. DdJ fabricated the nanowire device. YL and PK grew the InAs nanowires with an epitaxial aluminum shell. FKM wrote the manuscript with input from XXX

## ACKNOWLEDGMENTS

### Appendix A: Resonator model and extraction of $C_q$ and $G$

To extract the quantum capacitance,  $C$ , and the effective conductance,  $G$ , of the dot-island system, we measure the reflection from the resonant circuit comprised of the superconducting spiral inductor ( $L = 570$  nH), parasitic capacitance to ground, and the dot-island device itself. As illustrated in Fig. 1(b) the resonator losses and parasitic capacitance are treated as being in parallel to  $C$  and  $G$  of the device. The extraction of  $C$  and  $G$  requires the following:

1. the analytical resonator model, describing the complex reflection coefficient  $S_{11}$  as a function of the resonance frequency  $f_0$ , internal quality factor  $Q_{int}$  and number of other parameters;
2. analysis procedure for extracting  $f_0$  and  $Q_{int}$  from the measurement of  $S_{11}$ :
  - if the dependence of  $S_{11}(f)$  is measured explicitly, this role is performed by a nonlinear fit to the data;

- in case of the fixed-frequency measurement at known probing frequency  $f$ , it is achieved using the mapping  $S_{11} \mapsto f_0, Q_{int}$ , generated numerically based on the resonator model and an individual measurement of  $S_{11}(f)$ ;

3. conversion of changes in  $f_0$  and  $Q_{int}$  to  $C$  and  $G$ .

### 1. Resonator model

In our work we employ the resonator model described in detail in Ref. [23], and we only summarize it here. The model consists of three parts.

First, the resonator itself, modeled as an series RLC resonator coupled to a  $50 \Omega$  transmission line. Its reflection coefficient  $S'_{11}$  is given by

$$S'_{11}(f) = 1 - \frac{2Q_{load}Q_{ext}^{-1}}{1 + 2iQ_{load}\frac{(f-f_0)}{f_0}}, \quad (A1)$$

where  $f$  is the probing frequency,  $Q_{load} = (Q_{int}^{-1} + Q_{ext}^{-1})^{-1}$  – the loaded quality factor,  $Q_{int}$  – the internal quality factor,  $Q_{ext}$  – the external quality factor, and  $f_0$  – the resonance frequency.

Second element is the low-quality cavity, formed between the resonator and the partially reflective input of the cryogenic amplifier. The cavity modifies the measured signal, and can lead to the resonance asymmetry. The modified reflection coefficient is given by

$$S''_{11} = \frac{i\gamma\alpha\sqrt{1-\gamma^2}e^{-4\pi fli/c+i\phi}S'_{11}}{1-\sqrt{1-\alpha^2}(1-\gamma^2)e^{-4\pi fli/c+i\phi}S'_{11}}, \quad (A2)$$

where  $\gamma$  is the coupling coefficient of the used directional coupler,  $\alpha$  – amplifier reflection coefficient,  $l$  – length of the coaxial cables connecting the resonator with the amplifier, and  $c$  – propagation speed of the rf excitation in the coaxial cables.

Finally, global phase winding, phase offset and frequency-dependent amplification are taken into account phenomenologically, modifying the measured reflection coefficient

$$S_{11} = A \left( 1 + B \frac{f-f_0}{f_0} \right) \times e^{-ia+ib(f-f_0)} \times S''_{11}, \quad (A3)$$

where  $A \left( 1 + B \frac{f-f_0}{f_0} \right)$  accounts for a frequency-dependent attenuation and amplification, while  $e^{-ia+ib(f-f_0)}$  accounts for the phase shift.

For the procedure of fixing the numerous parameters in the model we refer the reader to the appendix of Ref. [23].

### 2. Conversion of fixed-frequency measurement to $f_0$ and $Q_{int}$

While the majority of the presented data is derived from the full resonator fit to the frequency-dependent



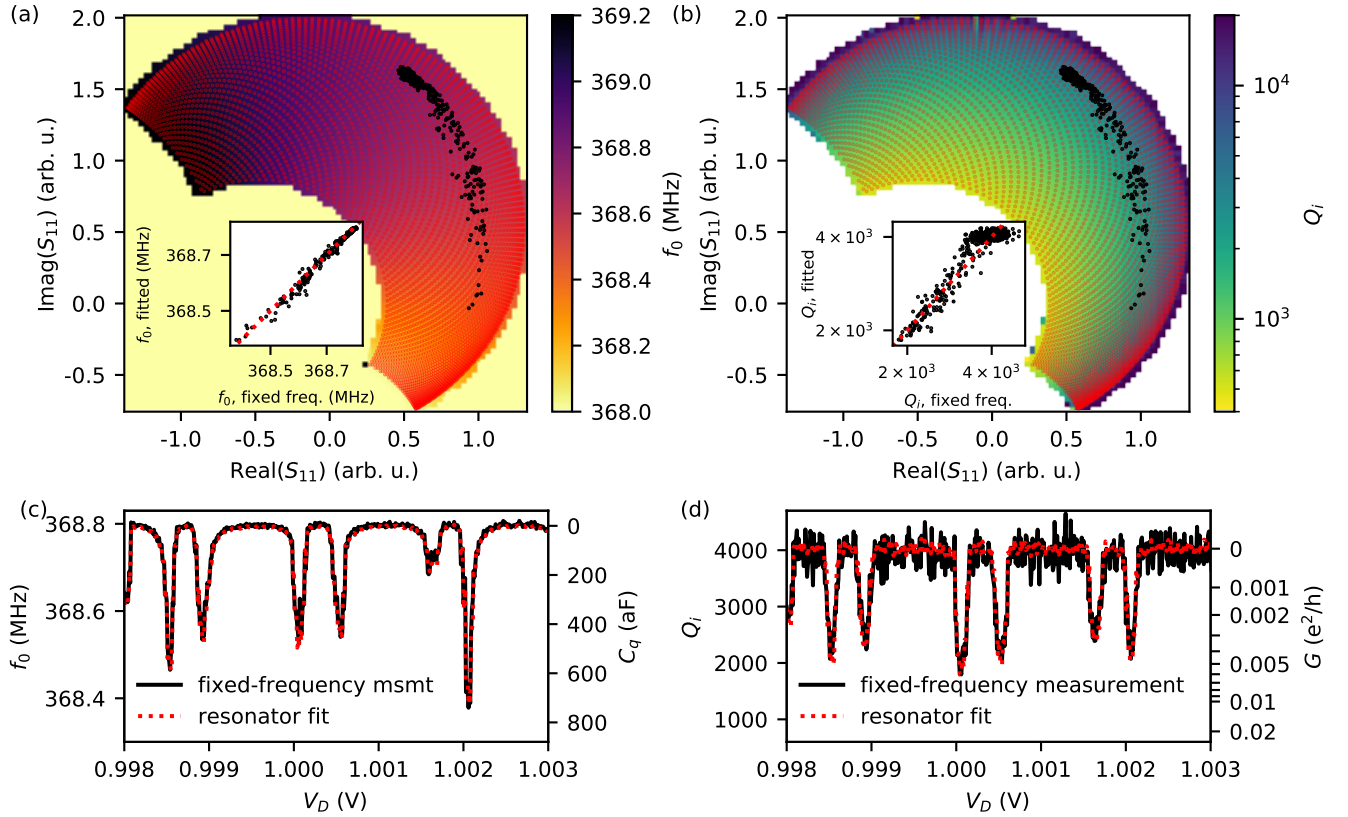


FIG. 4. (a,b) Mapping of the fixed-frequency measurement of  $S_{11}$  to  $f_0$  and  $Q_{int}$ , respectively. Red points indicate the grid of  $(f_0, Q_{int})$  used to generate the mapping. The actual grid was used 3 times more points than shown. Black points are indicate the scattered fixed-frequency data, from the data set corresponding to the green curve in Fig. 2(d) (c,d) Overlaid values of  $f_0$  and  $Q_{int}$ , extracted from the full resonator fit and the fixed-frequency measurements. Insets of (a,b) show correlations between the data sets in (c,d), with red dashed lines indicating  $x = y$ .

$S_{11}$ , the shown color maps (and cuts through them) rely on fixed-frequency measurement at the probing frequency  $f = 368.4$  MHz. In order to convert an individual measurement of the complex value of  $S_{11}$  to  $f_0$  and  $Q_{int}$  we apply the following procedure:

1. perform an individual, high-resolution measurement of  $S_{11}(f)$  and fit it with an analytical resonator model;
2. fix all of the model parameters, except for  $f_0$  and  $Q_{int}$ ;
3. evaluate the expected value of  $S_{11}$  for a dense grid of  $(f_0, Q_{int})$  values;
4. numerically invert the  $S_{11}(f_0, Q_{int})$  function to generate the mapping  $S_{11} \mapsto (f_0, Q_{int})$ ;
5. verify the uniqueness of the mapping in the relevant range of  $f_0$  and  $Q_{int}$  values
6. apply the mapping to the measured  $S_{11}$  at a fixed-frequency  $f$ .

Fig. 4 illustrates an example of the mapping  $S_{11} \mapsto (f_0, Q_{int})$ , based on a single resonator measurement from the full data set, corresponding to undepleted island in Fig. 2(d). In panels (a,b), color maps show the mapping, red points illustrate the grid of the  $(f_0, Q_{int})$  points, and black points are a scatter plot of  $S_{11}$  values measured at fixed probing frequency  $f$ , while tuning voltage  $V_D$ . The figure confirms that in the region of interest the mapping is unique. We note that due to the resonator asymmetry there is no range of  $f_0, Q_{int}$  for which the mapping  $S_{11} \mapsto (f_0, Q_{int})$  can be separated into two independent mappings,  $|S_{11}| \mapsto Q_{int}$  and  $\angle(S_{11}) \mapsto f_0$ .

Panels (c,d) compare extracted values of  $f_0, Q_{int}$  from the full resonator fit, and from the mapping of individual values of  $S_{11}(f)$  at  $f = 368.4$  MHz, from the same data set. We find that the values of  $f_0, Q_{int}$  agree between the two methods, except of much higher noise in case of fixed-frequency measurements. This observation is expected given that the effective integration time per point was two orders of magnitude shorter. The correlation between the  $f_0$  and  $Q_{int}$  values extracted with the two methods are presented in the insets of Fig. 4(a,b). An excellent correlation justifies the use of this extraction method of

$f_0$  and  $Q_{int}$  from the fixed-frequency measurement of  $S_{11}$  [(Fig. 2(a-c) and 8(a-c)].

### 3. Conversion of $f_0$ and $Q_{int}$ to $C$ and $G$

Having converted the measured reflection coefficients to  $f_0$  and  $Q_{int}$ , we establish their background values, i.e. the values  $f_0^{ref}$  and  $Q_{int}^{ref}$  corresponding to  $C = 0$  and  $G = 0$ . For every data set separately we use the mean of the values deep in the Coulomb blockade as a reference. Subsequently we calculate

$$C_q = \frac{1}{(2\pi f_0^{ref})^2 L} - \frac{1}{(2\pi f_0)^2 L}, \quad (A4)$$

using the nominal value of  $L = 570$  nH.

To obtain  $G$  we first calculate the characteristic impedance of the resonator  $Z_{ch} = 2\pi L f_0^{ref}$ . For a resonator model as in Fig. 1(b) the total conductance of the two resistors to ground (one representing losses in the resonator, another in the dot-island system) is given by  $G^{tot} = 1/Z_{char} Q_{int}$ . As in case of capacitance, we identify the value if conductance in the Coulomb blockade,  $G^{ref}$ , as representing the losses intrinsic to the resonator. Any increase of conductance above the reference level we attribute to the contribution of the dissipation in the dot-island:  $G = G^{tot} - G^{ref}$ .

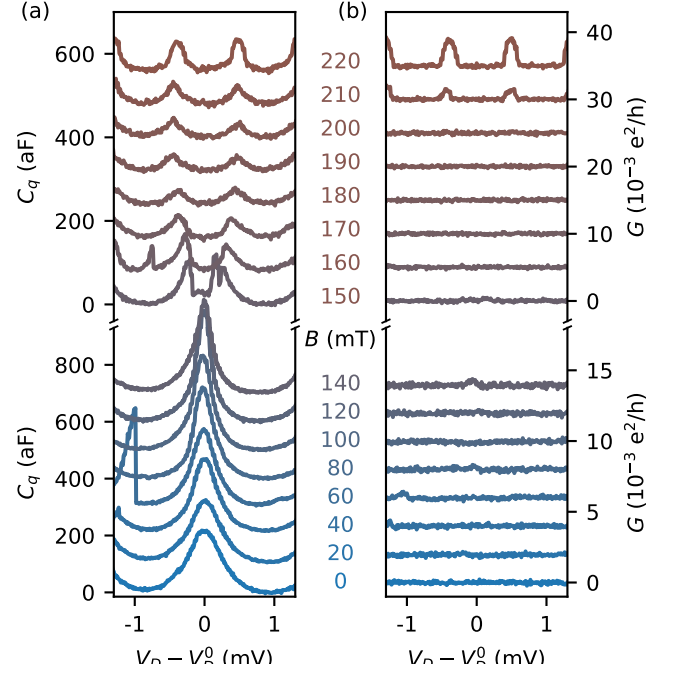


FIG. 6. ...

### Appendix B: Bx sweep

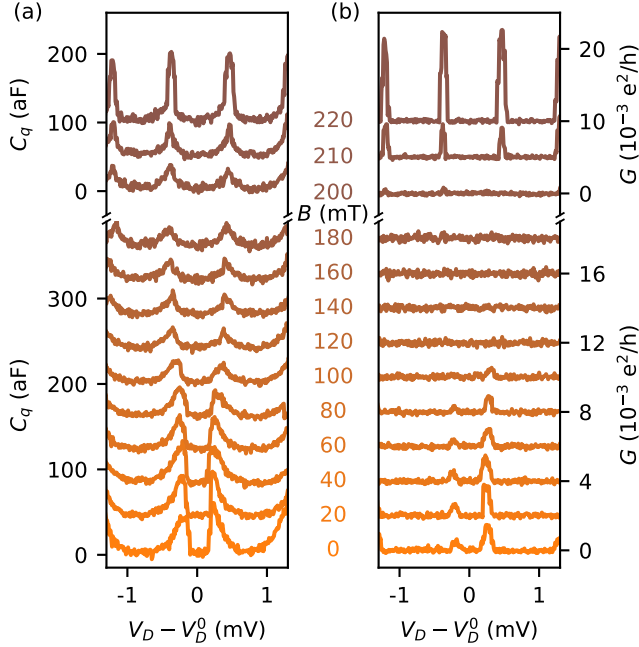


FIG. 5. ...

### Appendix C: Supplementary data

Fig. 8 presents extracted effective conductance of the dot island in the three regimes: depleted island and closed barrier, depleted island and open barrier, and undepleted island. These data sets correspond, panel-by-panel, to  $C$  presented in Fig. 2.



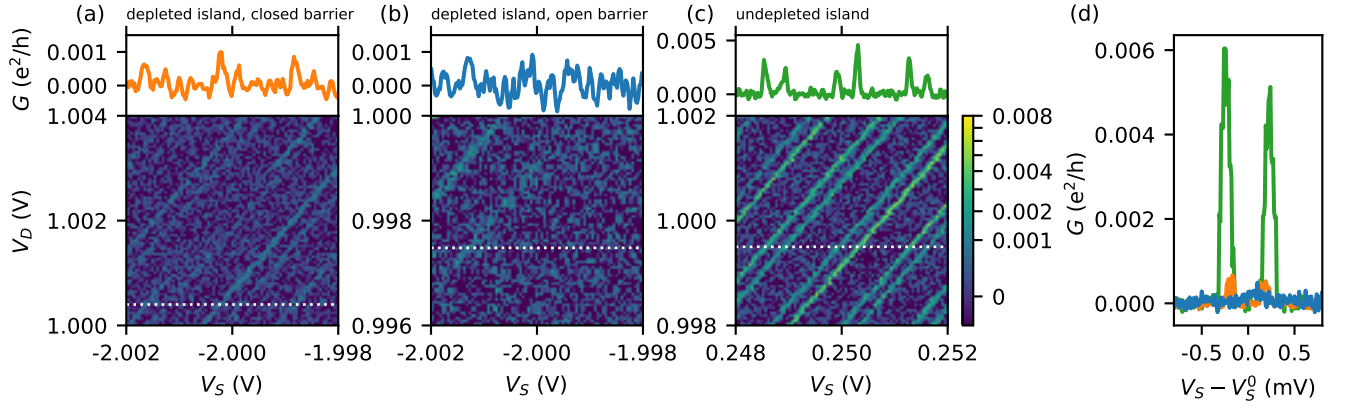


FIG. 7. Effective conductance a floating dot-island in three regimes, corresponding to the  $C$  measurements presented in Fig. 2. The three regimes in (a-c) are: (a) depleted semiconductor under aluminum shell and small tunnel coupling; (b) depleted semiconductor and large tunnel coupling; (c) undepleted semiconductor under the aluminum shell. Shared power-law normalization of color maps was chosen to enable direct comparison of datasets. Top panels show the cut through the data and use 3-point moving average to smooth the data. (d) Zoom in at an individual charge transition, or pair of charge transitions in the three regimes. The colors used for plotting the data correspond to the colors used in the top panels of (a-c).

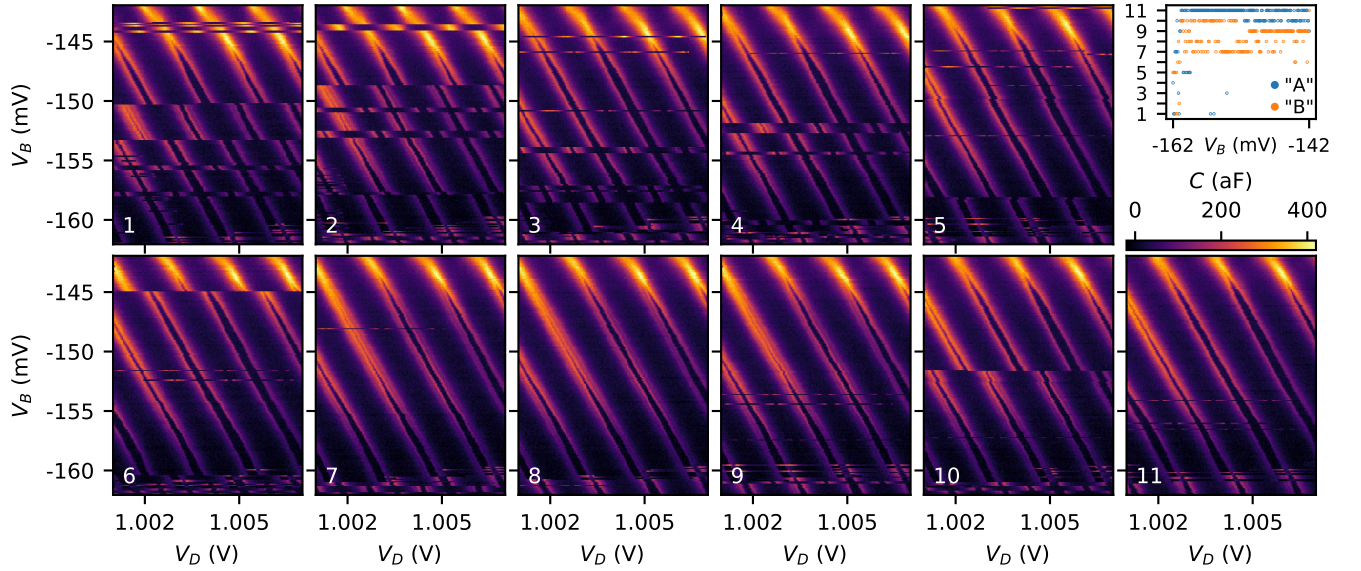


FIG. 8. XXX

- [1] L. Bretheau, Ç. Girit, H. Pothier, D. Esteve, and C. Urbina, Exciting andreev pairs in a superconducting atomic contact, *Nature* **499**, 312 (2013).
- [2] J. Pillet, C. Quay, P. Morfin, C. Bena, A. L. Yeyati, and P. Joyez, Andreev bound states in supercurrent-carrying carbon nanotubes revealed, *Nature Physics* **6**, 965 (2010).
- [3] E. J. Lee, X. Jiang, M. Houzet, R. Aguado, C. M. Lieber, and S. De Franceschi, Spin-resolved andreev levels and parity crossings in hybrid superconductor-semiconductor nanostructures, *Nature nanotechnology* **9**, 79 (2014).
- [4] A. Jellinggaard, K. Grove-Rasmussen, M. H. Madsen, and J. Nygård, Tuning yu-shiba-rusinov states in a quantum dot, *Physical Review B* **94**, 064520 (2016).
- [5] N. M. Chtchelkatchev and Y. V. Nazarov, Andreev quantum dots for spin manipulation, *Physical review letters* **90**, 226806 (2003).
- [6] M. Hays, V. Fatemi, D. Bouman, J. Cerrillo, S. Diamond, K. Serniak, T. Connolly, P. Krogstrup, J. Nygård, A. L. Yeyati, *et al.*, Coherent manipulation of an andreev spin qubit, *arXiv preprint arXiv:2101.06701* (2021).
- [7] J. C. E. Saldaña, A. Vekris, L. Pavešič, P. Krogstrup, R. Žitko, K. Grove-Rasmussen, and J. Nygård, Coulombic subgap states, *arXiv preprint arXiv:2101.10794* (2021).
- [8] D. Averin and Y. V. Nazarov, Single-electron charging of a superconducting island, *Physical review letters* **69**,

- 1993 (1992).
- [9] M. Tuominen, J. Hergenrother, T. Tighe, and M. Tinkham, Experimental evidence for parity-based 2e periodicity in a superconducting single-electron tunneling transistor, *Physical review letters* **69**, 1997 (1992).
  - [10] P. Krogstrup, N. Ziino, W. Chang, S. Albrecht, M. Madsen, E. Johnson, J. Nygård, C. M. Marcus, and T. Jespersen, Epitaxy of semiconductor–superconductor nanowires, *Nature materials* **14**, 400 (2015).
  - [11] J. Hornibrook, J. Colless, A. Mahoney, X. Croot, S. Blainvillain, H. Lu, A. Gossard, and D. Reilly, Frequency multiplexing for readout of spin qubits, *Applied Physics Letters* **104**, 103108 (2014).
  - [12] J. Van Veen, D. De Jong, L. Han, C. Prosko, P. Krogstrup, J. D. Watson, L. P. Kouwenhoven, and W. Pfaff, Revealing charge-tunneling processes between a quantum dot and a superconducting island through gate sensing, *Physical Review B* **100**, 174508 (2019).
  - [13] R. S. Deacon, A. Oiwa, J. Sailer, S. Baba, Y. Kanai, K. Shibata, K. Hirakawa, and S. Tarucha, Cooper pair splitting in parallel quantum dot josephson junctions, *Nature communications* **6**, 1 (2015).
  - [14] Z. Su, A. B. Tacla, M. Hoeschele, D. Car, S. R. Plissard, E. P. Bakkers, A. J. Daley, D. Pekker, and S. M. Frolov, Andreev molecules in semiconductor nanowire double quantum dots, *Nature communications* **8**, 1 (2017).
  - [15] J. E. Saldaña, A. Vekris, G. Steffensen, R. Žitko, P. Krogstrup, J. Paaske, K. Grove-Rasmussen, and J. Nygård, Supercurrent in a double quantum dot, *Physical review letters* **121**, 257701 (2018).
  - [16] J. E. Saldana, A. Vekris, R. Žitko, G. Steffensen, P. Krogstrup, J. Paaske, K. Grove-Rasmussen, and J. Nygård, Two-impurity yu-shiba-rusinov states in coupled quantum dots, *Physical Review B* **102**, 195143 (2020).
  - [17] A. Vekris, J. C. E. Saldaña, T. Kanne, M. Marnauza, D. Olsteins, F. Fan, X. Li, T. Hvid-Olsen, X. Qiu, H. Xu, *et al.*, Josephson junctions in double nanowires bridged by in-situ deposited superconductors, *arXiv preprint arXiv:2104.01591* (2021).
  - [18] H. Wu, P. Zhang, J. Stenger, Z. Su, J. Chen, G. Badawy, S. Gazibegovic, E. P. Bakkers, and S. M. Frolov, Triple andreev dot chains in semiconductor nanowires, *arXiv preprint arXiv:2105.08636* (2021).
  - [19] A. Y. Kitaev, Unpaired majorana fermions in quantum wires, *Physics-uspekhi* **44**, 131 (2001).
  - [20] J. D. Sau and S. D. Sarma, Realizing a robust practical majorana chain in a quantum-dot-superconductor linear array, *Nature communications* **3**, 1 (2012).
  - [21] I. C. Fulga, A. Haim, A. R. Akhmerov, and Y. Oreg, Adaptive tuning of majorana fermions in a quantum dot chain, *New journal of physics* **15**, 045020 (2013).
  - [22] D. Nozadze and N. Trivedi, Compressibility as a probe of quantum phase transitions in topological superconductors, *Physical Review B* **93**, 064512 (2016).
  - [23] F. K. Malinowski, L. Han, D. de Jong, J.-Y. Wang, C. G. Prosko, G. Badawy, S. Gazibegovic, Y. Liu, P. Krogstrup, E. P. Bakkers, *et al.*, Radio-frequency cv measurements with sub-attofarad sensitivity, *arXiv preprint arXiv:2110.03257* (2021).